Bioconjugate Chemistry

Article

pubs.acs.org/bc

Indocyanine Green-Loaded Nanoparticles for Image-Guided Tumor Surgery

Tanner K. Hill,[†,‡] Asem Abdulahad,[∥] Sneha S. Kelkar,[†,‡] Frank C. Marini,[‡,§] Timothy E. Long,[∥] James M. Provenzale,[⊥] and Aaron M. Mohs*[,†,‡,§]

[†]Virginia Tech − Wake Forest University School of Biomedical Engineering and Sciences, [‡]Wake Forest Institute for Regenerative Medicine, [§]Department of Cancer Biology, Wake Forest University Health Sciences, Winston-Salem, North Carolina 27157, United States;

[∥]Department of Chemistry, Virginia Polytechnic and State University, Blacksburg, Virginia 24061, United States;

[⊥]Department of Radiology, Duke Medical Center, Durham, North Carolina 27710, United States

Supporting Information

ABSTRACT: Detecting positive tumor margins and local malignant masses during surgery is critical for long-term patient survival. The use of image-guided surgery for tumor removal, particularly with near-infrared fluorescent imaging, is a potential method to facilitate removing all neoplastic tissue at the surgical site. In this study we demonstrate a series of hyaluronic acid (HLA)-derived nanoparticles that entrap the near-infrared dye indocyanine green, termed NanoICG, for improved delivery of the dye to tumors. Self-assembly of the nanoparticles was driven by conjugation of one of three hydrophobic moieties: aminopropyl-1-pyrenebutanamide (PBA), aminopropyl-5β-cholanamide (5βCA), or octadecylamine (ODA). Nanoparticle self-assembly, dye loading, and optical properties were characterized. NanoICG exhibited quenched fluorescence that could be activated by disassembly in a mixed solvent. NanoICG was found to be nontoxic at physiologically relevant concentrations and exposure was not found to inhibit cell growth. Using an MDA-MB-231 tumor xenograft model in mice, strong fluorescence enhancement in tumors was observed with NanoICG using a fluorescence image-guided surgery system and a whole-animal imaging system. Tumor contrast with NanoICG was significantly higher than with ICG alone.

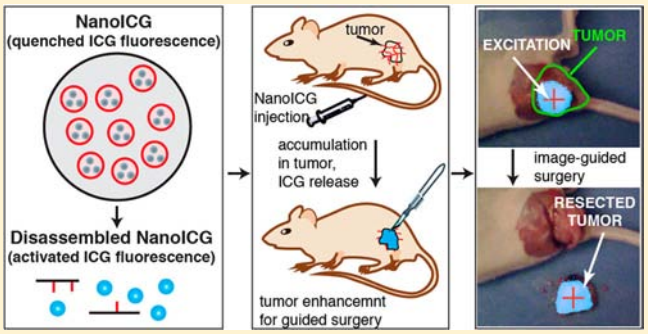

INTRODUCTION

Surgery is one of the most common and effective forms of cancer treatment. Surgical treatment is utilized in a large percentage of cases of solid tumors; for example, between 63% and 98% of lung, bladder, breast cancer, and colorectal cancer patients undergo surgery, depending on type and grade.[1] Tumor recurrence resulting from positive margins, local metastases, metastatic lymph nodes, and other forms of neoplastic tissue that go undetected during the surgical procedure is a significant factor in both disease-free survival and long-term survival. For example, approximately 30% of breast cancer patients experience either local or systemic disease recurrence.[2,3] This results, in part, from the high incidence of positive margins in breast conserving surgery, reported to be 20−40%.[4] Thus, complete removal of all neoplastic tissue at the surgical site greatly improves patient survival.

Current methods of detecting tumor margins intraoperatively involve palpation and visual inspection, which are characterized by poor tissue contrast and spatial resolution and lack a means to detect nonpalpable lesions.[5,6] Traditional imaging modalities such as radiography, MRI, PET, SPECT, and ultrasound (US), typically involve instrumentation that is too cumbersome or dangerous to use in the surgical theater, or are incapable of providing tumor-specific information with high contrast or resolution.[7]

More recently, fluorescence-based image-guided surgery (IGS) has shown great potential to intraoperatively detect tumors. Near infrared (NIR) imaging in combination with NIR fluorescent contrast agents utilizes wavelengths in the range of 700−900 nm and is of particular interest because minimal autofluorescence from native tissue is present in this range, allowing a high signal-to-background ratio. Furthermore, excitation light at these wavelengths has excellent tissue penetration, thereby providing a means to detect contrast material at a depth of several millimeters within tissue.[8] Several NIR IGS systems are already commercially available or have been examined in clinical settings[9,10] and fluorescence-based IGS has shown preclinical success using in vivo models.[11−15] Clinically, fluorescence-based IGS has been used to map

Received: December 3, 2014
Revised: January 6, 2015
Published: January 7, 2015

DOI: 10.1021/bc5005679
Bioconjugate Chem. 2015, 26, 294−303

Scheme 1[a]

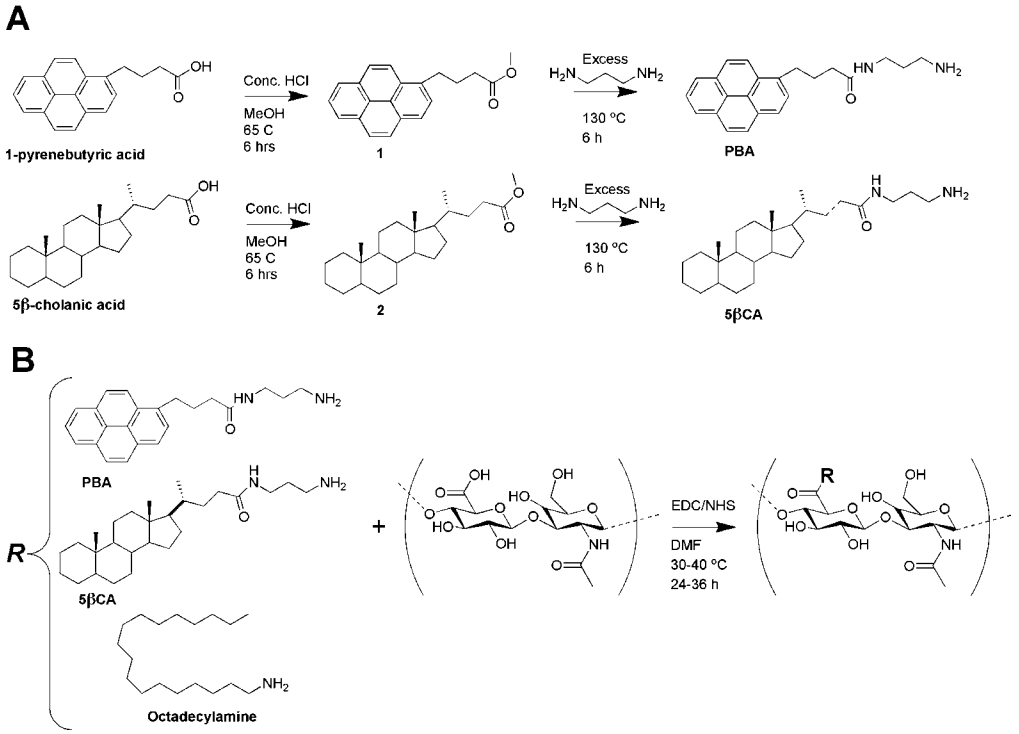

[a](A) Synthesis of hydrophobic amides using 1-pyrenebutyric acid 5-β-cholanic acid involves addition of methanol (MeOH) followed by substitution with 1,3 diaminopropane. (B) Conjugation of hydrophobic moieties, PBA, 5βCA, or ODA, to HLA via EDC/NHS reaction.

sentinel lymph nodes of tumors arising from the breast, skin, gastrointestinal tract, lung, and other sites.[16−18] Furthermore, this technique has been used for intraoperative imaging of solid tumors using either nonspecific agents (e.g., in hepatobiliary tumors and breast cancer[17]) or tumor-specific agents (e.g., in ovarian cancer).[19]

IGS systems require a NIR fluorescent contrast agent that can accumulate in a tumor. Several studies have utilized the FDA-approved exogenous NIR fluorophore, indocyanine green (ICG), to detect human tumor xenografts in mice,[20] spontaneous tumors in companion canines,[21,22] and for investigative human trials involving detection of solid tumor or sentinel lymph nodes.[17,18] ICG does, however, have a relatively short circulation half-life, 150−180 s,[23] which can limit the total amount delivered to a tumor and ultimately reduce contrast enhancement. In addition, ICG has been shown to have limitations in discerning malignant from benign tissue or inflammatory tissue.[21]

Encapsulation of ICG within a NP formulation has been shown to increase circulation time[24−26] and facilitate delivery to tumors.[27−30] In this study, we report the development of a series of self-assembled nanoparticles based on hydrophobically modified hyaluronic acid (HLA) conjugates that noncovalently entrap ICG. HLA is a natural, biodegradable, and hydrophilic biopolymer capable of self-assembly after conjugation to hydrophobic groups, which has previously enabled the delivery of therapeutics and imaging agents to tumors.[31−34] HLA is an extracellular polysaccharide composed of β(1,4) D-glucuronic acid and β(1,3) N-acetyl-D-glucosamine that is normally associated with extracellular matrix and is a ligand for CD44, which is overexpressed in many human tumors[35] and has been linked to increased tumor invasiveness.[35−38] Furthermore, HLA can be hydrolyzed by hyaluronidases, in particular, HYAL-1 and HYAL-2, which have increased expression and activity in breast cancer and prostate cancer.[39,40] Herein, we optimized ICG loading by tuning the physical and chemical properties of HLA using three distinct hydrophobic moieties: aminopropyl-1-pyrenebutanamide (PBA), aminopropyl-5β-cholanamide (5βCA), and octadecylamine (ODA), to drive self-assembly of HLA polymers into NPs and to entrap ICG within the NPs. The resulting nanoparticles, termed NanoICG, were evaluated for physical, chemical, and optical properties. Select NanoICG formulations were evaluated for in vitro toxicity, tumor accumulation, and image-guided surgery. To study NanoICG as an image-guided surgery (IGS) contrast agent, an IGS system was used that employs a hand-held probe for wavelength-resolved NIR fluorophore detection;[13] the hand-held probe simultaneously provides a directed, laser excitation source for a widefield video-rate camera system for intuitive surgical detection of the contrast agent.[22]

RESULTS AND DISCUSSION

Hydrophobic Moiety Synthesis and Conjugation to HLA. Three structurally distinct hydrophobic moieties were examined to determine their effect on driving self-assembly and ICG loading. 5-β-Cholanic acid and ODA have previously been reported to successfully drive self-assembly when conjugated to HLA,[33,41,42] while PBA has not been previously conjugated to HLA. 1-Pyrenebutyric acid and 5-β-cholanic acid were refluxed in methanol to give **1** and **2**, respectively. Next, methyl esters, **1** and **2**, were converted to amide products, PBA and 5βCA, respectively, by refluxing 1,3-diaminopropane as shown in Scheme 1A. PBA and 5βCA each possess a primary amine moiety for conjugation to HLA. Since PBA is previously unreported, mass spectra and ^{1}H NMR of this product are shown in Figure 1A,B. The structural characterization of 5βCA

DOI: 10.1021/bc5005679
Bioconjugate Chem. 2015, 26, 294−303

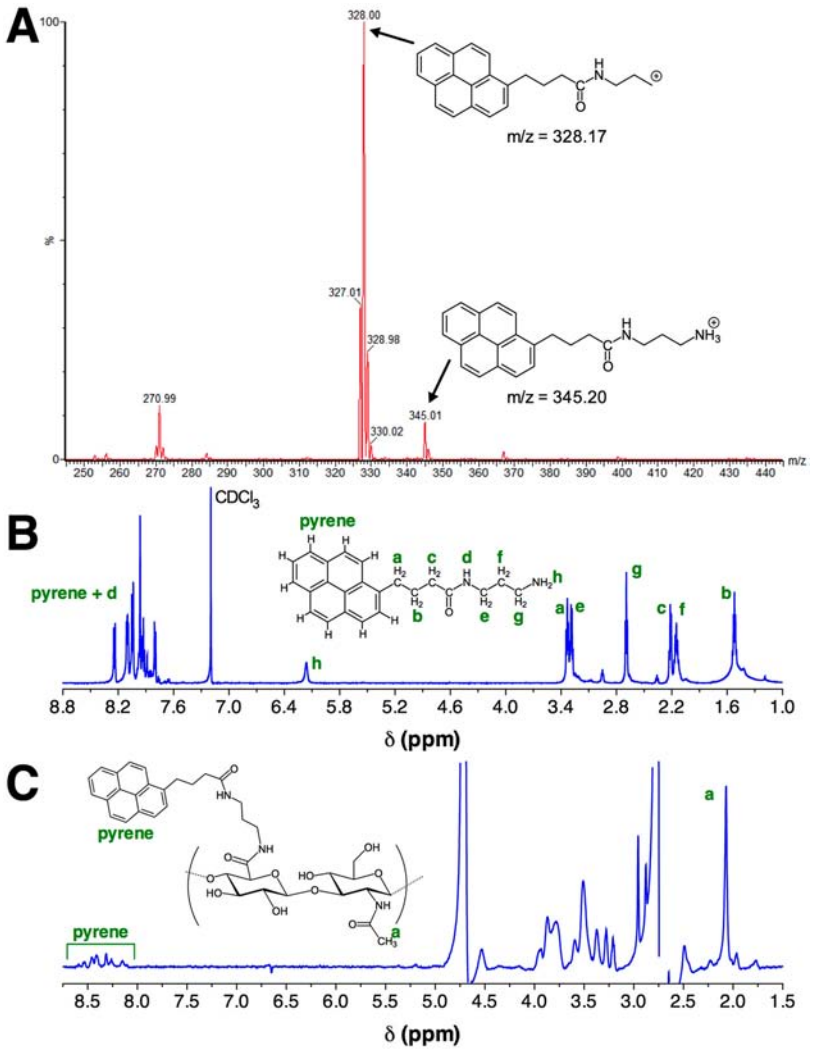

Figure 1. Mass spectrometry (A) and ^{1}H NMR (B) confirmed the synthesis of PBA. (C) Quantification of conjugation of PBA to hyaluronic acid was achieved by calculating the ratio of aromatic pyrene protons relative to the *N*-acetyl protons (a) on *N*-acetyl-D-glucosamine of hyaluronic acid. Mass spectrometry and ^{1}H NMR of 5βCA and ODA derivatives can be found in Supporting Information Figure 1.

is shown in Supporting Information Figure 1. ODA was used as provided for conjugation to HLA. Conjugation of the primary amine group on PBA, 5βCA, or ODA to the carboxylic acid group of the glucuronic acid moiety was performed using 1-ethyl-3-[3-(dimethylamino)propyl]carbodiimide hydrochloride (EDC) and *N*-hydroxysuccinimide (NHS) chemistry to facilitate amide bond formation (Scheme 1B).

Conjugation of the hydrophobic groups to HLA was performed using loading ratios of 5 wt % (Low) and 10 wt % (High) for PBA-HLA and 5βCA-HLA, and 2.5 wt % for ODA-HLA. Conjugation ratios with greater than 2.5 wt % ODA had poor solubility and did not form NPs efficiently, while reducing the wt % of ODA lowers the ligand-to-polymer ratio below 1:1. Successful conjugation was observed for all products in the NMR spectra (Figure 1C, Supporting Information Figure S1). This synthesis produced amphiphilic HLA polymers with varying degrees of substitution of hydrophobic moieties. Such amphiphilic conjugates were necessary to drive self-assembly and provide a hydrophobic domain for entrapment of ICG, as schematically depicted in Figure 2A. Conjugation degree and ICG loading efficiencies are shown in Table 1.

It was hypothesized that PBA could provide increased loading efficiency for ICG compared 5βCA or ODA, because of the potential for $\pi-\pi$ stacking between PBA and ICG.[43] ODA is capable of efficient self-association, but is not structurally similar to ICG. Each wt % of PBA and 5βCA conjugates was found to load more ICG than ODA-HLA; ODA-HLA loading was 13−35% less compared to the other hydrophobic moieties. ICG loading into PBA-HLA NPs was equal to or higher than 5βCA-HLA. Loading efficiency (33−50%) and ICG content (6−10 wt %) of NanoICG were moderate compared to previous ICG-loaded NP formulations,[44,45] which range from very low loading efficiency (1−10%) and content (0.16−0.21 wt %) to moderate,[26,27] and relatively high efficiencies of 34−97% and content up to 23%.[46] NanoICG with maximum ICG content was used in order to minimize the total mass of nanoparticle required for injection.

Physical, Chemical, and Optical Characterization. Hydrodynamic diameters of empty NPs (i.e., those not loaded with ICG) ranged from 150 to 260 nm, whereas NanoICG formulations ranged from 80 to 150 nm depending on the hydrophobic group (Figure 2B, Supporting Information Figure S2). NPs were observed at all concentrations within the

DOI: 10.1021/bc5005679
Bioconjugate Chem. 2015, 26, 294−303

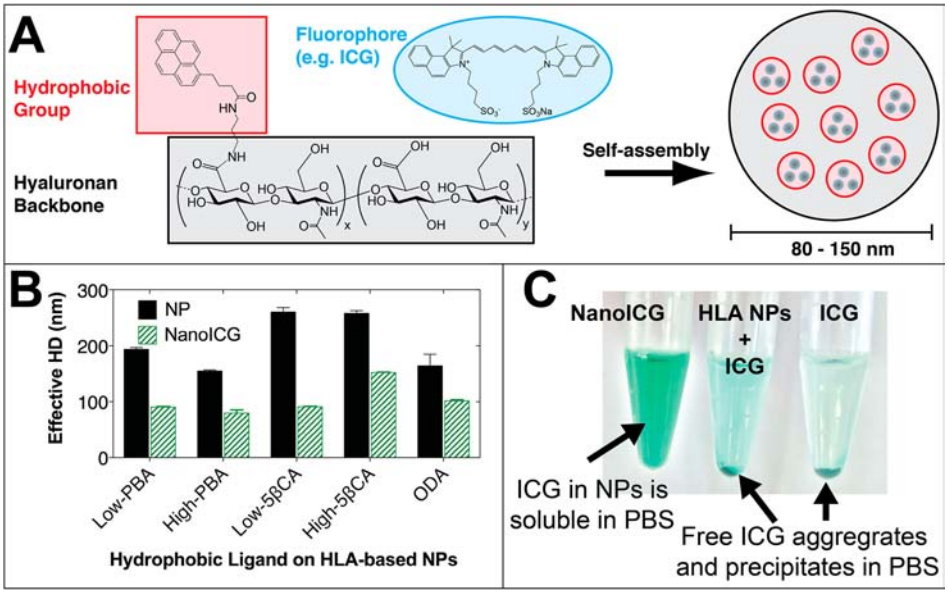

Figure 2. (A) Hydrophobic moieties conjugated to HLA drive self-assembly into nanoparticles that can entrap ICG. (B) NP diameters range from 80 to 260 nm, with smaller diameters observed in NanoICG formulations. (C) NanoICG formulations increase ICG solubility in aqueous salt solution by providing a favorable electrostatic environment, while ICG alone or not entrapped in NPs has poor solubility and precipitates rapidly.

Table 1. Characterization and ICG Loading of HLA Conjugates

sample	theoretical hydrophobic moiety conjugation mol %[a]	actual hydrophobic moiety conjugation mol %[b]	ICG loading efficiency[c]	ICG wt %	fluorescence activation[d]
Low-PBA-HLA	5.8	5.67	0.501 ± 0.004	10.0 ± 0.1%	4.47
High-PBA-HLA	12.2	10.1	0.470 ± 0.004	9.4 ± 0.1%	2.08
Low-5βCA-HLA	4.8	3.88	0.370 ± 0.003	7.4 ± 0.1%	6.52
High-5βCA-HLA	10.1	6.0	0.475 ± 0.004	9.5 ± 0.1%	11.62
ODA-HLA	2.8	2.77	0.327 ± 0.003	6.5 ± 0.1%	12.29

[a]Molar loading ratio. [b]Calculated molar loading ratio determined by NMR integration. [c]ICG loading efficiency = (calculated ICG concentration measured by absorbance spectroscopy)/(theoretical concentration based on loading amount). [d]Fluorescence activation = [integrated fluorescence intensity (790–950 nm) of NanoICG in 1:1 DMSO:H_2O]/[integrated fluorescence intensity (790–950 nm) of NanoICG in H_2O].

detection limits of the instruments used in this study. NanoICG formulations increased the solubility of ICG in PBS, as was observed by an optically transparent green color throughout the PBS solution; centrifugation could not remove ICG from solution. The same quantity of ICG alone or ICG mixed with previously assembled NPs in PBS was insoluble and could be pelleted by centrifugation (Figure 2C). The size of NanoICG remained consistent in FBS (see Supporting Information Figure S3).

The absorbance and fluorescence spectra of ICG in DMSO showed peaks near 800 and 825 nm, respectively (Figure 3A). The extinction spectra of NanoICG showed strong scattering in pure water and PBS, likely due to aggregation and electronic effects of ICG,[43] suggesting the ICG was self-associated within the NPs (Figure 3B). NanoICG fluorescence was quenched in aqueous solution (Figure 3B). NanoICG disassembly was induced by the addition of DMSO. The resulting absorbance and fluorescent spectra of ICG closely resembled its characteristic shape (Figure 3C), suggesting dye release. The fluorescence signal after DMSO addition over the quenched state for each NanoICG formulation is shown in Table 1. All NPs investigated showed strong quenching and activation (Supporting Information Figure S3). Change in the absorption peak of ICG, indicative of scattering by NPs, is consistent with

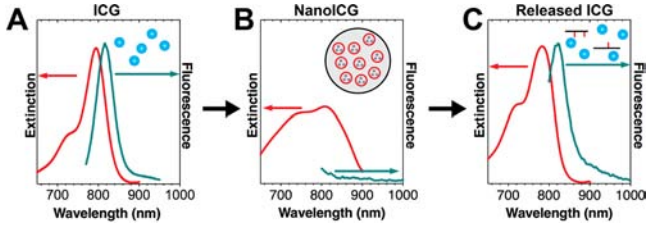

Figure 3. (A) ICG dissolved in DMSO shows clear absorbance and fluorescence peaks near 800 and 825 nm, respectively. (B) Nanoparticle formulations of ICG show broadened absorbance spectra with a less discernible peak due to scattering by NP-entrapped ICG, and ICG fluorescence is quenched. (C) NPs disassemble in 50:50 DMSO:H_2O, decreasing the scattering in ICG absorbance and fluorescence activation, which demonstrates the potential for optical property control.

previous reports.[45,46] However, the fluorescence quenching observed in NanoICG (Supporting Information Figure S4) is observed in only some formulations of encapsulated ICG,[45,47] but not others.[30] Nanoparticle entrapment of ICG did provide a modest, yet significant increase in the photostability of ICG compared to free ICG (Supporting Information Figure S5).

DOI: 10.1021/bc5005679
Bioconjugate Chem. 2015, 26, 294–303

The photoprotective effect is consistent with dyes closely associated in a matrix.[48]

Interestingly, when ICG was entrapped, the NP diameter decreased, regardless of the hydrophobic conjugate. These data suggest that the hydrophobic groups of amphiphilic HLA facilitates close association of ICG. Close packing of ICG in NPs is further supported by the optical and colloidal properties of NanoICG. First, the absorbance peaks of ICG, when loaded into NPs, showed a decreased signal at ~795 nm and an increased scattering contribution to extinction spectra (Figure 3B) when compared to ICG in DMSO (Figure 3A). These findings are consistent with previously reported results.[42,49] Second, fluorescence quenching was also observed in NanoICG formulations. Finally, ICG becomes stable in high salt conditions when associated with amphiphilic HLA conjugates. Taken together, the findings of the broad absorbance of NanoICG, self-quenched fluorescence, and increased ICG salt stability strongly suggest that ICG is being closely associated within NPs via sequestration in hydrophobic domains. It is important to note that precise control of quenching and activation may also prove useful for image-guided surgery if high levels of fluorescence activation can be achieved specifically in the tumor environment.[46,50] Indeed, our research team is currently investigating precise control of fluorescence activation of HLA-derived nanoparticles.

Cytotoxicity Analysis. MS-1 mouse endothelial cells were chosen to represent mouse vasculature upon introduction of NPs. All NPs and NanoICG formulations did not affect the metabolic activity of these cells at physiologically relevant concentrations (i.e., 5−50 μg/mL of ICG) using a CCK-8 assay, as shown in Figure 4A. Because High-PBA-HLA NanoICG was found to have the smallest effective diameter and approximately equivalent or higher ICG loading than other NPs, these were further investigated for their cytotoxicity to MDA-MB-231 breast cancer cells. Proliferation of MDA-MB-231 cells was not hindered after a 24 h exposure to High-PBA-HLA NanoICG, suggesting that the NPs do not have a detrimental effect on target cell populations (Figure 4B). The results are analogous to the cytotoxicity profiles of other nanoparticle formulations of ICG.[30,45]

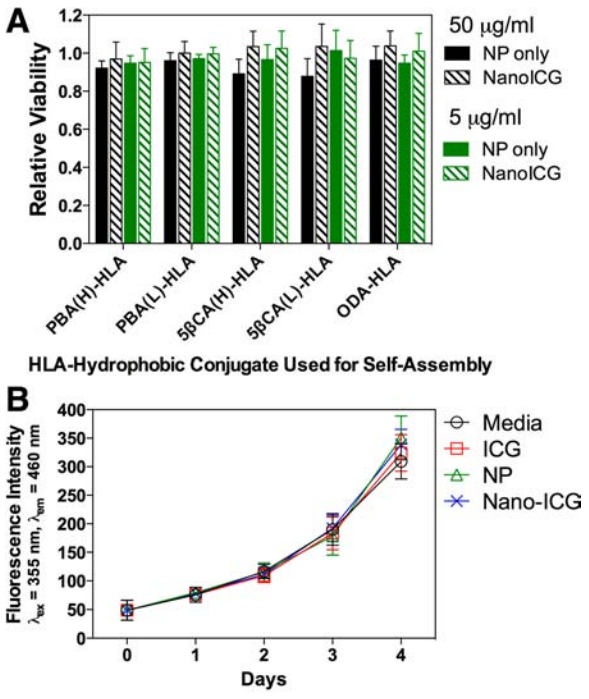

Figure 4. (A) Cell metabolic assay showed that NPs with and without ICG have cytotoxicity that is comparable relative to control cells. (B) Treatment of MDA-MB-231 cells with 5 μg/mL High-PBA-HLA NP did not impact subsequent proliferation as determined by a DNA quantification assay.

In Vivo Tumor and Organ Accumulation. iRFP-labeled MDA-MB-231 human tumor xenografts were grown subcutaneously in female nude mice. When tumors were sufficiently large, mice were injected with either ICG in water (i.e., the standard clinical method) or the High-PBA-HLA NanoICG formulation. Mice were euthanized 24 h after injection and imaged with a LI-COR Pearl Impulse small animal imaging system and an image-guided surgery system.[13,22] Figure 5A shows the signal-to-noise ratios (SNRs) of resected tissues analyzed using the small animal imaging system. Compared to ICG, NanoICG resulted in substantially higher signal in tumor, although the difference was not statistically significant (p = 0.088). The fluorescence due to ICG did not significantly differ in other tissues ($p \geq 0.78$). The combination of higher signal in tumor, but similar background in surrounding tissue, resulted in a significantly higher contrast to noise ratio (CNR) in mice that were administered NanoICG compared to ICG alone (p = 0.037) as shown in Figure 5B. The average CNR in NanoICG-treated mice was more than twice that of mice treated with free ICG (91 vs 40). This is an important distinction, as it is CNR, rather than SNR, that allows for more robust discrimination of tumor from normal tissue using IGS. The relative biodistribution of NanoICG at 24 h was consistent with previous results of nanoparticle encapsulated ICG, i.e., showing the highest signal in liver and kidneys with higher signal in the tumor compared to surrounding tissues.[27−30,51] The majority of ICG accumulated in the liver for both NanoICG and free ICG formulations, which is consistent with ICG clearance.[52,53] While no significant difference was observed between the SNR of similar tissues, NanoICG exhibited lower kidney and muscle

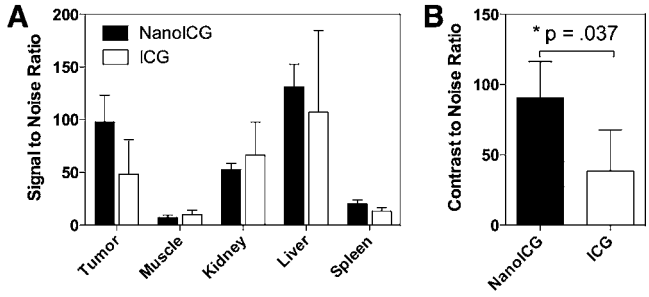

Figure 5. (A) Biodistribution of ICG 24 h after injection as measured by SNR. Liver accumulated the majority of ICG from both formulations, followed by kidney. NanoICG and ICG SNR were not found to be significantly different in the tested tissues, although the NanoICG signal was higher in tumor tissue (p = 0.088; N = 5 mice/group). (B) The contrast-to-noise ratio (CNR) between tumor and surrounding muscle was significantly higher in NanoICG-treated tumors, suggesting that the NanoICG formulation improved the potential for distinguishing between tumor and normal tissue. *$p \leq$ 0.05 was considered significant, SNR = (signal of tissue)/($SD_{background}$); CNR = (Tumor − Muscle)/($SD_{background}$). Representative NIR emission images from ICG and NanoICG are shown in Supporting Information Figure S6.

DOI: 10.1021/bc5005679
Bioconjugate Chem. 2015, 26, 294−303

accumulation, and higher liver and spleen accumulation than free ICG. The comparable overall SNR from ICG and NanoICG is indicative of some degree of ICG dissociation from the NPs. The higher liver and spleen signal from NanoICG may indicate some interaction with resident macrophage. The statistically significant CNR values between ICG and NanoICG in tumor indicate that NanoICG has distinctly different biodistribution compared to free ICG. These results are likely independent of NanoICG dose. A recent report demonstrates that ICG that was directly conjugated to poly(ethylene glycol) grafted-HLA, where ICG served as the hydrophobic ligand, resulted in tumor signal, both fluorescence and photoacoustic, that was more than double that of femur.[54] However, the dose of ICG used in this study, 50 nmol per mouse, was 5 times greater than the dose used in this study.

Image-Guided Surgery. Small animal florescence imaging, provided by LI-COR Pearl Impulse system, indicated iRFP fluorescence (700 nm channel; false-colored red) that was consistent with the location of the iRFP-labeled MDA-MB-231 cells; a representative example is shown in Figure 6A. Using the separate IGS system,[13,22] directed laser excitation (785 nm) of the tumor produced strong fluorescence enhancement due to the presence of ICG (Figure 6B; false-colored cyan), which corresponded to the boundaries of iRFP-labeled tumor cells observed in Figure 6A. Laser excitation of surrounding normal skeletal muscle showed no fluorescent signal based on a predetermined threshold (Figure 6C).[13] Subsequently, the tumor was debulked under IGS using fluorescence enhancement from NanoICG. Figure 6D shows the presence of ICG in the resected tumor mass. A region of tissue that fluorescently enhanced at the tumor/normal tissue interface during IGS could not be excised because removal was restricted by the presence of bone (Figure 6E). However, subsequent 700 nm imaging (in the whole animal imaging system) and histological analysis after animal necropsy revealed that this fluorescence-enhancing region was due to tumor infiltration into normal tissue (Figure 6E,F). Further investigations are planned to determine NanoICG's ability to enhance specifically at the tumor margin. Analysis of the debulked tissue and mouse carcass with whole animal fluorescence imaging at 700 nm to detect iRFP-labeled MDA-MB-231 cells (shown in Figure 6F) confirmed the fluorescence enhancement detected in tumor by IGS.

The image-guided tumor surgery study reported here, removal a breast tumor xenograft in mice with image-guidance, demonstrates the potential of NanoICG to depict tumor margins in the operating room. The colocalization of ICG signal and iRFP-labeled MDA-MB-231 tumor cells establishes that ICG delivery to tumors using NanoICG was successful and indicated the tumor boundaries. The strong contrast enhancement in the tumor showed that more ICG was delivered to tumors by NPs with lower background signal in surrounding tissue, which could provide meaningful data to surgeons in the operating room. In combination, these results suggest that use of NanoICG could potentially serve as a contrast agent for IGS.

Ultimately, one could envision using NanoICG and with image-guided surgery to determine surgical margins. However, determining the tumor margin is complex. Currently, a positive margin is determined by the presence of neoplastic cells at the edge of the excised tumor. These can be detected by intraoperative pathology and definitively by IHC after the surgery. There is no method currently available to detect tumor cells remaining in the surgical cavity. Using xenograft tumor models in mice, while useful to evaluate overall SNR and tumor contrast, has physical and biological limitations. With the resolution of optical imaging methodologies being approximately 0.1 × 0.1 mm^2,[7,22] this gives the level of contrast agent distribution and signal necessary for effective surgical removal. Further investigation will be required to determine how the

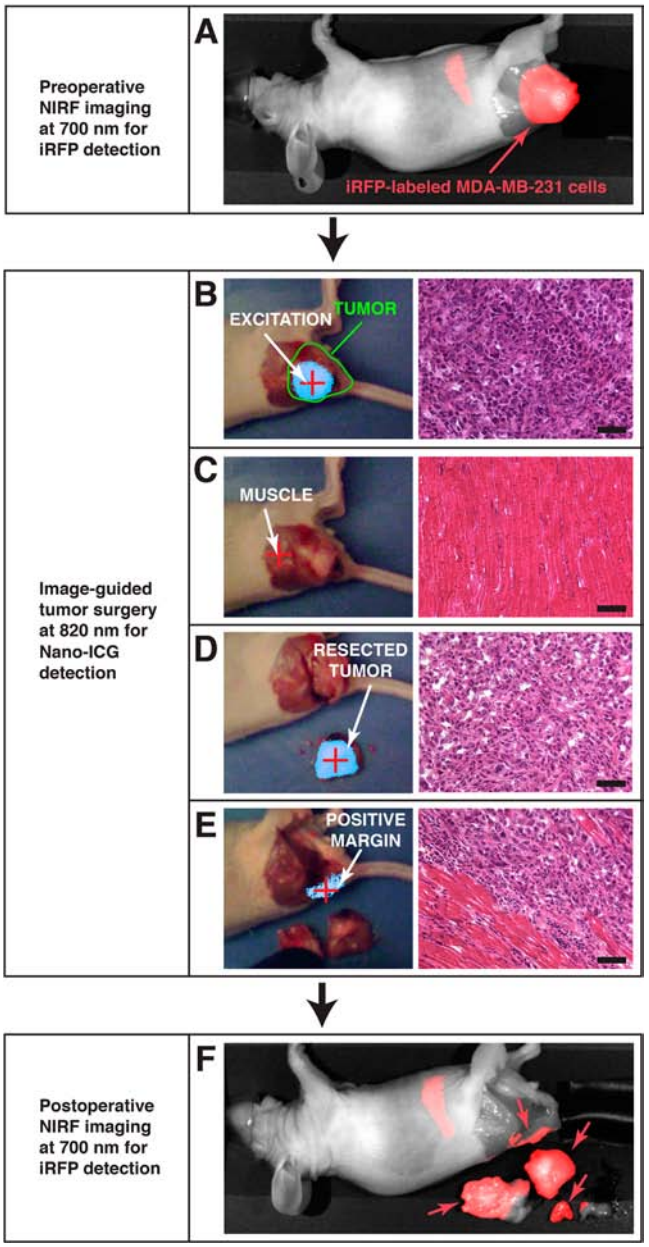

Figure 6. In vivo analysis of NanoICG tumor accumulation. (A) Preoperative imaging of iRFP shows the location of MDA-MB-231 breast tumor xenograft; the signal in the abdomen is due to rodent chow in the intestinal tract. (B) Image-guided surgery (left) and H&E histological staining (right) confirm high fluorescent signal in the bulk of the tumor, (C) while only low fluorescent signal is observed in adjacent normal tissue. (D) The resected tumor exhibits fluorescent signal; presence of tumor was confirmed at histology. Tumor margins were then inspected for fluorescent enhancement to confirm tumor removal. (E) Fluorescence was detected at the tumor margin, suggesting remaining tumor tissue. (F) Positive margins were confirmed by observing iRFP signal at the location indicated by the presence of NanoICG.

DOI: 10.1021/bc5005679
Bioconjugate Chem. 2015, 26, 294−303

intratumoral biodistribution affects the surgeon's ability detect surgical margins by image-guided surgery.

The mechanism of ICG release to transition from a quenched to an unquenched state is likely the result of release of ICG from NPs to serum proteins and lipids or degradation via hyaluronidases. The comparable overall biodistribution of NanoICG to ICG in nontumor tissues indicates that ICG exchanges from NanoICG to serum proteins to some extent. Intratumoral degradation by hyaluronidases provides an additional mechanism for tumor-specific fluorescence activation, but differentiating these effects will require additional investigation. The potential maximum detection depth of tumors underlying healthy tissue is likely to be between 5 and 10 mm.[7,13,22] However, a number of factors will influence this depth. Volume and fluid distribution within the tumor will strongly affect the level of contrast agent uptake and thus total signal and imaging depth.[55] The number of cells in a tumor may influence fluorescence signal indirectly by affecting tumor size and vascularity, and therefore total contrast agent uptake.

■ CONCLUSIONS

The potential to use IGS in treatment of operable tumors is clear: improved detection of tumors and their boundaries could minimize recurrent disease. In this study NPs derived from HLA were used to deliver the NIR fluorophore ICG in an attempt to improve contrast enhancement. The nanoparticles developed here readily entrapped ICG and were not toxic in cell culture. Nanoparticle formulations of ICG produced stronger contrast enhancement compared to free ICG. Our team is actively investigating the serum stability and release profile of ICG from NanoICG. Ultimately, the efficacy of NanoICG will need to be established to determine if the increased contrast enhancement in IGS results in decreased tumor recurrence after IGS.

■ EXPERIMENTAL PROCEDURES

1-Pyrenebutyric acid, octadecylamine, 5-β-cholanic acid, 1,3-diaminopropane, *N*-hydroxy succinimide, and 1-ethyl-3-(3-(dimethylamino)propyl)carbodiimide (EDC), indocyanine green (ICG), and fetal bovine serum (FBS) were obtained from Sigma-Aldrich (St. Louis, MO). Unless otherwise noted, all water was obtained from a Barnstead NANOpure Diamond (Thermo Scientific; Waltham, MA) system producing 18.2 MΩ water. Sodium hyaluronate was purchased from Lifecore Biomedical (Chaska, MN). Methanol and *N*,*N*-dimethylformamide (DMF) were purchased from Fisher Scientific (Pittsburgh, PA). Ethanol was purchased from the Warner-Graham Company (Cockeysville, MD). Matrigel was purchased from BD Biosciences (San Jose, CA). Penicillin/streptomycin and other media reagents were purchased from ATCC (Manassas, VA).

Aminopropyl-5-β-Cholanamide Synthesis. 5-β-cholanic methyl ester was prepared according to the methods described in the literature.[32] Briefly, in a 25 mL round-bottom flask (RBF), 5-β-cholanic acid (2.8 mmol, 1.0 mg) was dissolved in 5 mL methanol. To the RBF, 180 μL of concentrated HCl was then added under stirring and this solution was allowed to reflux at 60−65 °C for 6 h. The product was cooled to 0 °C and appeared as a white precipitate. The precipitate was collected under vacuum filtration, washed with cold methanol, and then dried under vacuum. 0.80 mg of 5-β-cholanic methyl ester was recovered (2.1 mmol, 75% yield). 5βCA was synthesized by dissolving 5-β-cholanic methyl ester (1.36 mmol, 0.51 mg) in 132 mmol (~11 mL) of 1,3-diaminopropane. This solution was refluxed at 130 °C for 6 h and then allowed to cool to 0 °C. 5βCA was obtained from crystallization with water. The white precipitate was then washed with 200 mL cold nanopure water under vacuum filtration and dried under vacuum to produce 0.952 mmol (0.397 mg, 70% yield).

Aminopropyl-1-Pyrenebutanamide Synthesis. 1-Pyrenebutyric acid (1.93 mmol, 558 mg) was dissolved in 5.5 mL MeOH with 3% concentrated HCl and refluxed for 6 h at 60−65 °C. The reaction solution produced two layers: the top layer was clear and light yellow, while the bottom layer was dark and oil-like. The top layer was removed and the product, 1-pyrenebutyric methyl ester, was confirmed in the bottom layer and dried under vacuum. 1-Pyrenebutyric methyl ester (0.881 mmol, 266.4 mg) was then dissolved into 6 mL 1,3-diaminopropane and refluxed at 130 °C for 6 h to produce a clear, brown liquid. This solution was then cooled to 0 °C and PBA was precipitated by cold water, washed in cold water, and dried under vacuum. This process produced 0.52 mmol (180 mg, 59% yield).

Conjugation of 5βCA or PBA to Hyaluronic Acid. Sodium hyaluronate (90−95 mg, M_N = 10−20 kDa) was dissolved in 25 mL of water. PBA at 5 or 10 wt % (14 or 28 mmol, 5 or 10 mg), or 5βCA at 5 or 10 wt % (12 or 24 mmol, 5 or 10 mg), was dissolved into 25 mL DMF under stirring at 30−40 °C. NHS and EDC, 78−154 mmol (10× molar ratio to PBA or 5βCA), were then dissolved into the HLA solution. The PBA or 5βCA DMF solution was then added dropwise to the activated HLA solution under constant stirring. The reaction was allowed to stir until completion at room temperature, 24−36 h. The reaction contents were then transferred to dialysis tubing (material: MWCO = 3500 Da, Spectrum Laboratories) and allowed to dialyze against 1:1 EtOH:H_2O for 24 h followed by H_2O for an additional 48 h. The polymer−hydrophobic moiety conjugate was removed from the dialysis tubing and lyophilized for storage at −20 °C. This process produced High-PBA-HLA (10 wt % PBA), Low-PBA-HLA (5 wt % PBA), High-5βCA-HLA (10 wt % 5βCA), and HLow-5βCA-HLA (5 wt % 5βCA).

Conjugation of Octadecylamine to HLA. ODA (9.3 mmol, 2.5 mg) was dissolved into a 70% EtOH:H_2O solution. HLA, 97.5 mg, was dissolved into a separate solution of 70% EtOH:H_2O and 10-fold molar excess of EDC and NHS were then added. The ODA solution was then added slowly into the HLA solution under vigorous stirring and the reaction was allowed to proceed for 24−36 h at room temperature. The reaction mixture was then dialyzed (material, MWCO = 3500 Da, Spectrum Laboratories) against 1:1 EtOH: H_2O for 24 h and water alone for 48 h. This material, ODA-HLA (2.5 wt % ODA), was then lyophilized and stored at −20 °C.

Polymer Conjugate Characterization. The PBA and 5βCA intermediate methyl ester products were analyzed by GC-MS with a Thermo Scientific Trace Ultra gas chromatograph interfaced with a Thermo Scientific TSQ Quantum XLS (Thermo Scientific; Waltham, MA) using splitless injection. Separation was performed on a 10.4 m DB-1 WCOT column (Agilent Technologies Inc.; Santa Clara, CA). PBA and 5βCA were analyzed on a Waters Q-Tof API-US mass spectrometer with Advion TriVerso NanoMate (Advion Biosystems; Ithaca, NY) using positive ion electrospray. 5βCA-HLA, PBA-HLA, and ODA-HLA conjugates were analyzed on a Bruker Avance 600 MHz NMR spectrometer with TXI Cryoprobe at 25 °C,

DOI: 10.1021/bc5005679
Bioconjugate Chem. 2015, 26, 294−303

with 64 to 128 scans, 8192 to 16 384 data points, and 10−12 s relaxation delay. 5βCA-HLA and PBA-HLA were analyzed in 50/50 D_2O/DMSO-D_6 (D_2O from Acros Organics "100.0%" D, Fisher Scientific, DMSO-D_6 from Cambridge Isotope Laboratories, 99.9% D). Data was processed in Mnova NMR (Escondido, CA).

ICG Loading into Nanoparticles. Amphiphilic HLA polymer conjugate, 8−16 mg, was dissolved in 5 mL of water, while ICG (0.0026−0.0052 mmol, 2.0−4.0 mg) was dissolved in 5 mL DMSO and added to HLA solution. This solution was vortexed and then dialyzed against H_2O for 24−36 h to remove DMSO and drive self-assembly of ICG-entrapped NPs. Resulting NPs were then filtered through a PD-10 desalting column (GE Lifesciences; Pittsburgh, PA) to remove free ICG. The clear green solution was then lyophilized until resuspension of NPs. Materials produced by this process are termed High-PBA-NanoICG, Low-PBA-NanoICG, High-5βCA-NanoICG, Low-5βCA-NanoICG, and ODA-NanoICG.

Nanoparticle Characterization. NanoICG or empty NPs (empty NPs underwent the same dialysis treatment, but without ICG) were diluted to a concentration of 0.1 mg/mL in PBS and filtered through a 0.45 um filter (Fisher Scientific; Pittsburgh,PA). The hydrodynamic diameter (HD) of the NP-containing solutions was determined on ZetaPlus system with an onboard dynamic light scattering (DLS) analyzer (Brookhaven Instruments Corporation; Holtsville, NY). Absorbance (extinction) spectra were obtained on a UV-2600 (Shimadzu Scientific Instruments; Columbia MD). Fluorescence spectra were obtained on a FluoroMax-4 fluorescence spectrometer equipped with a NIR extended range PMT (Horiba Jobin Yvon; Edison, NJ). Spectra were obtained on aqueous solutions containing NPs and disassembled NP contents by addition of an equal volume of DMSO. ICG-loading content was determined with absorbance spectroscopy with a standard curve of ICG in 1:1 H_2O/DMSO.

Cytotoxicity. Cytotoxicity was evaluated by CCK-8 assay (Dojido, Japan). 2000 MS1 mouse endothelial cells were seeded into 96 well plates and allowed to adhere for 24 h in EMEM (Gibco), 10% FBS (Sigma-Aldrich), 1% P/S (Gibco). Cells were then mixed with normal media containing High-PBA-HLA, High-PBA-NanoICG, Low-PBA-HLA, Low-PBA-NanoICG, 5βCA-HLA, 5βCA-NanoICG, ODA-HLA, or ODA-NanoICG at concentrations of 50 and 5 μg/mL. Cells were incubated for 24 h followed by analysis with CCK-8 assay. Proliferation of MDA-MB-231 cells was analyzed using a FluoReporter Blue DNA quantification assay (Life Technologies; Grand Island, NY). 2×10^3 MDA-MB-231 cells were seeded into wells of tissue-treated 96 well plates. The cells were exposed to High-PBA-HLA or High-PBA-NanoICG at 5 μg/mL, for 24 h. After the 24 h exposure standard media was applied. DNA was quantified at 0, 24, 48, 72, and 96 h.

iRFP Transfection of MDA-MB-231 Cells. Amplification of iRFP plasmid (piRFP 31857, Addgene, Cambridge, MA) was performed by PCR using Platinum High Fidelity PCR SuperMix (Invitrogen cat#12532016) and custom designed primers. Primers were designed to include 15bp of homology to the LentiX Bicistronic Expression System (puro) from Clontech (Cat #632183) in order to perform ligation utilizing In-Fusion HD cloning (Clontech #639645). Agarose gel electrophoresis of PCR product was resolved, excised, and purified using Infusion spin column PCR purification kit. The LentiX Bicistronic vector was linearized using EcoR1, resolved by agarose, excised, and gel purified. For ligation of iRFP into the lentix vector, the Infusion Cloning was carried out using 5× Infusion HD Enzyme mix, transformed, plated, and colonies selected. Restriction Enzyme Digest was performed to check for orientation of the product. Positive clones were verified and used to produce lentiviral supernatants. To make lentivirus, the Lenti-X HTX packaging system (Clontech) was used with Lenti-X 293T cells, and virus production was verified using Lenti-X GoStix. MDA-MB-231 cells were transduced using 0.5 mL of lentiviral supernatant with 8 μg/mL Polybrene in DMEM media for 48 h, virus removed, and drug selected for stable cell lines using 5 μg/mL puromycin for 5 days.

Near Infrared Fluorophore Enhanced Image-Guided Surgery. Breast tumor xenografts were introduced into 12−14-week-old female athymic nude mice (Jackson Laboratories; Bar Harbor, ME) by the subcutaneous injection of 2×10^6 iRFP MDA-MB-231 cells in 50/50 media/matrigel. When the tumors reached 500−1000 mm^3, mice were injected with an intravenous infusion via a tail vein of either ICG or High-PBA-NanoICG (10 nmol ICG total) in 200 μL water (N = 5 mice/group). The quantities of ICG in both the free ICG and High-PBA-NanoICG solutions were determined by dissolving a fraction in 1:1 H_2O/DMSO and acquiring the absorbance spectrum, followed by making the appropriate dilutions to achieve 10 nmol/200 μL as determined by an ICG standard curve. Absorbance spectra of both free ICG and High-PBA-NanoICG were analyzed and diluted to equal absorbance values prior to injection. Mice were euthanized 24 h after injection of NIR fluorescent contrast agents and the mice were imaged using a Pearl Impulse Small Animal Imaging System (LI-COR Biosciences; Lincoln, NE). Tumors were then removed using a separate image-guided surgery system that has been previously described.[13,22] In brief, skin was removed to visually inspect identifiable tumor tissue. Next, the portable fluorescence spectrometer with a fiber-coupled hand-held (SciApps; Laramie, WY) unit was used to detect NIR emission from the tumor. The laser also served as the directed excitation source for a wide-field NIR imaging system (SpectroPath Image-Guided Surgery System; Atlanta, GA) that merges NIR and color channels and provides real-time video feedback for the surgeon. Using the IGS system, tumor boundaries were first highlighted and then underwent a debulking procedure. Image-guided resection of enhancing regions was iteratively performed until either no fluorescence signal was observed at the tumor margin or debulking was no longer possible. Mice were then re-imaged on the LI-COR whole-animal imaging system for comparison of iRFP fluorescence emission from the MDA-MB-231 tumor cells (700 nm channel) with fluorescence emission from ICG (800 nm channel). Tumor, muscle, kidney, liver, and spleen were harvested and underwent further fluorescence imaging. Using LI-COR software, tumor to muscle contrast was determined by generating an area of interest (AOI) around each tumor and corresponding muscle sample. The average signal intensities of these AOIs were then used to calculate contrast: CNR = (Tumor − Muscle)/($SD_{background}$). Biodistribution was analyzed using the signal-to-noise ratio (SNR) of target tissues and organs: SNR = Tissue/($SD_{background}$). Histological analysis was performed with H&E staining.

Statistical Analysis. Analyses of average NP size, ICG loading, and cytotoxicity were performed with one-way ANOVA. Organ biodistribution and tumor contrast between free ICG and High-PBA-NanoICG mice were performed with Student's t test. All statistical analyses were done in Prism 6.0 (GraphPad Software; La Jolla, CA) and Excel.

DOI: 10.1021/bc5005679
Bioconjugate Chem. 2015, 26, 294−303

■ ASSOCIATED CONTENT

Supporting Information

Chemical characterization of 5bCA- and ODA-HLA conjugates. Dynamic light scattering histograms are available for each conjugate with and without loaded ICG. Absorbance and fluorescence emission spectra are reported for nanoparticle in aqueous and DMSO:H_2O. Serum protein interaction, photo stability, and tissue imaging studies are reported. This material is available free of charge via the Internet at http://pubs.acs.org.

■ AUTHOR INFORMATION

Corresponding Author

*E-mail: amohs@wakehealth.edu. Tel: (336) 713-1326. Fax: (336) 713-7296.

Notes

The authors declare the following competing financial interest(s): Dr. Mohs is an inventor of instrumentation related to this manuscript, which has been licensed to Spectropath, Inc. and may be subject to royalties and shares associated with the technology.

■ ACKNOWLEDGMENTS

This work was supported in part by the National Institutes of Health (R00 CA153916 and R01 EB019449 to A.M.M.), Wake Forest Institute for Regenerative Medicine and WFU-VT SBES. We especially thank D.A. Horita for his expertise and assistance with NMR acquisition and analysis. The Waters Q-TOF mass spectrometer was purchased with funds from NIH Shared Instrumentation Grant 1S10RR17846 and the Thermo Electron TSQ Quantum XLS GC/MS/MS from NIH Shared Instrumentation Grant 1S10RR027940. We thank the Mass Spectrometer Facility and the Cell and Viral Vector Core Laboratory for their services, which are supported by the Comprehensive Cancer Center of Wake Forest University NCI CCSG P30CA012197 grant.

■ ABBREVIATIONS

HLA, hyaluronic acid/hyaluronan; ICG, indocyanine green; NP, nanoparticle; NanoICG, hyaluronic acid derived nanoparticle that entrap ICG; IGS, image-guided surgery; PBA, aminopropyl-1-pyrenebutanamide; 5βCA, aminopropyl-5β-cholanamide; ODA, octadecylamine

■ REFERENCES

(1) Siegel, R., DeSantis, C., Virgo, K., Stein, K., Mariotto, A., Smith, T., Cooper, D., Gansler, T., Lerro, C., Fedewa, S., Lin, C., Leach, C., Cannady, R. S., Cho, H., Scoppa, S., Hachey, M., Kirch, R., Jemal, A., and Ward, E. (2012) Cancer treatment and survivorship statistics, 2012. *CA Cancer J. Clin. 62*, 220−241.

(2) Meric, F., Mirza, N., Vlastos, G., Buchholz, T., Kuerer, H., Babiera, G., Singletary, S., Ross, M., Ames, F., Feig, B., Krishnamurthy, S., Perkins, G., McNeese, M., Strom, E., Valero, V., and Hunt, K. (2003) Positive surgical margins and ipsilateral breast tumor recurrence predict disease-specific survival after breast-conserving therapy. *Cancer 97*, 926−933.

(3) Wapnir, I. L., Dignam, J. J., Fisher, B., Mamounas, E. P., Anderson, S. J., Julian, T. B., Land, S. R., Margolese, R. G., Swain, S. M., Costantino, J. P., and Wolmark, N. (2011) Long-term outcomes of invasive ipsilateral breast tumor recurrences after lumpectomy in NSABP B-17 and B-24 randomized clinical trials for DCIS. *J. Natl. Cancer Inst. 103*, 478−488.

(4) Jacobs, L. (2008) Positive margins: the challenge continues for breast surgeons. *Ann. Surg. Oncol. 15*, 1271−1272.

(5) Lovrics, P. J., Cornacchi, S. D., Vora, R., Goldsmith, C. H., and Kahnamoui, K. (2011) Systematic review of radioguided surgery for non-palpable breast cancer. *Eur. J. Surg. Oncol. 37*, 388−397.

(6) van der Ploeg, I. M., Hobbelink, M., van den Bosch, M. A., Mali, W. P., Borel Rinkes, I. H., and van Hillegersberg, R. (2008) 'Radioguided occult lesion localisation' (ROLL) for non-palpable breast lesions: a review of the relevant literature. *Eur. J. Surg. Oncol. 34*, 1−5.

(7) Frangioni, J. (2008) New technologies for human cancer imaging. *J. Clin. Oncol. 26*, 4012−4021.

(8) Frangioni, J. (2003) In vivo near-infrared fluorescence imaging. *Curr. Opin. Chem. Biol. 7*, 626−634.

(9) Gioux, S., Choi, H. S., and Frangioni, J. V. (2010) Image-guided surgery using invisible near-infrared light: fundamentals of clinical translation. *Mol. Imaging 9*, 237−255.

(10) Troyan, S. L., Kianzad, V., Gibbs-Strauss, S. L., Gioux, S., Matsui, A., Oketokoun, R., Ngo, L., Khamene, A., Azar, F., and Frangioni, J. V. (2009) The FLARE intraoperative near-infrared fluorescence imaging system: a first-in-human clinical trial in breast cancer sentinel lymph node mapping. *Ann. Surg. Oncol. 16*, 2943−2952.

(11) Cai, W., Shin, D., Chen, K., Gheysens, O., Cao, Q., Wang, S., Gambhir, S., and Chen, X. (2006) Peptide-labeled near-infrared quantum dots for imaging tumor vasculature in living subjects. *Nano Lett. 6*, 669−676.

(12) de Grand, A. M., and Frangioni, J. V. (2003) An operational near-infrared fluorescence imaging system prototype for large animal surgery. *Technol. Cancer Res. Treat. 2*, 553−562.

(13) Mohs, A. M., Mancini, M. C., Singhal, S., Provenzale, J. M., Leyland-Jones, B., Wang, M. D., and Nie, S. (2010) Hand-held spectroscopic device for in vivo and intraoperative tumor detection: contrast enhancement, detection sensitivity, and tissue penetration. *Anal. Chem. 82*, 9058−9065.

(14) Parungo, C., Ohnishi, S., Kim, S.-W., Kim, S., Laurence, R., Soltesz, E., Chen, F., Colson, Y., Cohn, L., Bawendi, M., and Frangioni, J. (2005) Intraoperative identification of esophageal sentinel lymph nodes with near-infrared fluorescence imaging. *J. Thorac. Cardiovasc. Surg. 129*, 844−850.

(15) Winer, J. H., Choi, H. S., Gibbs-Strauss, S. L., Ashitate, Y., Colson, Y. L., and Frangioni, J. V. (2010) Intraoperative localization of insulinoma and normal pancreas using invisible near-infrared fluorescent light. *Ann. Surg. Oncol. 17*, 1094−1100.

(16) Kim, S., Lim, Y. T., Soltesz, E. G., De Grand, A. M., Lee, J., Nakayama, A., Parker, J. A., Mihaljevic, T., Laurence, R. G., Dor, D. M., Cohn, L. H., Bawendi, M. G., and Frangioni, J. V. (2004) Near-infrared fluorescent type II quantum dots for sentinel lymph node mapping. *Nat. Biotechnol. 22*, 93−97.

(17) Schaafsma, B. E., Mieog, J. S. D., Hutteman, M., van der Vorst, J. R., Kuppen, P. J. K., Löwik, C. W. G. M., Frangioni, J. V., van de Velde, C. J. H., and Vahrmeijer, A. L. (2011) The clinical use of indocyanine green as a near-infrared fluorescent contrast agent for image-guided oncologic surgery. *J. Surg. Oncol. 104*, 323−332.

(18) van der Vorst, J. R., Schaafsma, B. E., Verbeek, F. P., Keereweer, S., Jansen, J. C., van der Velden, L. A., Langeveld, A. P., Hutteman, M., Lowik, C. W., van de Velde, C. J., Frangioni, J. V., and Vahrmeijer, A. L. (2013) Near-infrared fluorescence sentinel lymph node mapping of the oral cavity in head and neck cancer patients. *Oral Oncol. 49*, 15−19.

(19) van Dam, G. M., Themelis, G., Crane, L. M. A., Harlaar, N. J., Pleijhuis, R. G., Kelder, W., Sarantopoulos, A., de Jong, J. S., Arts, H. J. G., van der Zee, A. G. J., Bart, J., Low, P. S., and Ntziachristos, V. (2011) Intraoperative tumor-specific fluorescence imaging in ovarian cancer by folate receptor-α targeting: first in-human results. *Nat. Med. 18*, 1315−1319.

(20) Altinoğlu, E. I., Russin, T. J., Kaiser, J. M., Barth, B. M., Eklund, P. C., Kester, M., and Adair, J. H. (2008) Near-infrared emitting fluorophore-doped calcium phosphate nanoparticles for in vivo imaging of human breast cancer. *ACS Nano 2*, 2075−2084.

DOI: 10.1021/bc5005679
Bioconjugate Chem. 2015, 26, 294−303

(21) Holt, D., Okusanya, O., Judy, R., Venegas, O., Jiang, J., DeJesus, E., Eruslanov, E., Quatromoni, J., Bhojnagarwala, P., Deshpande, C., Albelda, S., Nie, S., and Singhal, S. (2014) Intraoperative near-infrared imaging can distinguish cancer from normal tissue but not inflammation. *PLoS One 9*, e103342.
(22) Mohs, A. M., Mancini, M. C., Provenzale, J. M., Saba, C. F., Cornell, K. K., Howerth, E. W., and Nie, S. An integrated widefield imaging and spectroscopy system for contrast enhanced, image-guided resection of tumors. *IEEE Trans. Biomed. Eng.* Accepted for publication.
(23) Shimizu, S., Kamiike, W., Hatanaka, N., Yoshida, Y., Tagawa, K., Miyata, M., Matsuda, H. (1995) New method for measuring ICG Rmax with a clearance meter. *World J. Surg. 19*, 113−118; discussion 118.
(24) Ma, Y., Tong, S., Bao, G., Gao, C., and Dai, Z. (2013) Indocyanine green loaded SPIO nanoparticles with phospholipid-PEG coating for dual-modal imaging and photothermal therapy. *Biomaterials 34*, 7706−7714.
(25) Saxena, V., Sadoqi, M., and Shao, J. (2006) Polymeric nanoparticulate delivery system for Indocyanine green: biodistribution in healthy mice. *Int. J. Pharm. 308*, 200−204.
(26) Yaseen, M. A., Yu, J., Jung, B., Wong, M. S., and Anvari, B. (2009) Biodistribution of encapsulated indocyanine green in healthy mice. *Mol. Pharmaceutics 6*, 1321−32.
(27) Ganesh, S., Iyer, A. K., Gattacceca, F., Morrissey, D. V., and Amiji, M. M. (2013) In vivo biodistribution of siRNA and cisplatin administered using CD44-targeted hyaluronic acid nanoparticles. *J. Controlled Release 172*, 699−706.
(28) Makino, A., Kizaka-Kondoh, S., Yamahara, R., Hara, I., Kanzaki, T., Ozeki, E., Hiraoka, M., and Kimura, S. (2009) Near-infrared fluorescence tumor imaging using nanocarrier composed of poly(L-lactic acid)-block-poly(sarcosine) amphiphilic polydepsipeptide. *Biomaterials 30*, 5156−5160.
(29) Miki, K., Oride, K., Inoue, S., Kuramochi, Y., Nayak, R. R., Matsuoka, H., Harada, H., Hiraoka, M., and Ohe, K. (2010) Ring-opening metathesis polymerization-based synthesis of polymeric nanoparticles for enhanced tumor imaging in vivo: Synergistic effect of folate-receptor targeting and PEGylation. *Biomaterials 31*, 934−942.
(30) Zheng, C., Zheng, M., Gong, P., Jia, D., Zhang, P., Shi, B., Sheng, Z., Ma, Y., and Cai, L. (2012) Indocyanine green-loaded biodegradable tumor targeting nanoprobes for in vitro and in vivo imaging. *Biomaterials 33*, 5603−5609.
(31) Cho, H.-J., Yoon, H. Y., Koo, H., Ko, S.-H., Shim, J.-S., Lee, J.-H., Kim, K., Kwon, I. C., and Kim, D.-D. (2011) Self-assembled nanoparticles based on hyaluronic acid-ceramide (HA-CE) and Pluronic® for tumor-targeted delivery of docetaxel. *Biomaterials 32*, 7181−7190.
(32) Choi, K. Y., Min, K. H., Na, J. H., Choi, K., Kim, K., Park, J. H., Kwon, I. C., and Jeong, S. Y. (2009) Self-assembled hyaluronic acid nanoparticles as a potential drug carrier for cancer therapy: synthesis, characterization, and in vivo biodistribution. *J. Mater. Chem. 19*, 4102−4107.
(33) Choi, K. Y., Yoon, H. Y., Kim, J.-H., Bae, S. M., Park, R.-W., Kang, Y. M., Kim, I.-S., Kwon, I. C., Choi, K., Jeong, S. Y., Kim, K., and Park, J. H. (2011) Smart nanocarrier based on PEGylated hyaluronic acid for cancer therapy. *ACS Nano 5*, 8591−8599.
(34) El-Dakdouki, M. H., Zhu, D. C., El-Boubbou, K., Kamat, M., Chen, J., Li, W., and Huang, X. (2012) Development of multifunctional hyaluronan-coated nanoparticles for imaging and drug delivery to cancer cells. *Biomacromolecules 13*, 1144−1151.
(35) Zöller, M. (2011) CD44: can a cancer-initiating cell profit from an abundantly expressed molecule? *Nat. Rev. Cancer 11*, 254−267.
(36) Abraham, B. K., Fritz, P., McClellan, M., Hauptvogel, P., Athelogou, M., and Brauch, H. (2005) Prevalence of CD44+/CD24−/low cells in breast cancer may not be associated with clinical outcome but may favor distant metastasis. *Clin. Cancer Res. 11*, 1154−1159.
(37) Al-Hajj, M., Wicha, M. S., Benito-Hernandez, A., Morrison, S. J., and Clarke, M. F. (2003) Prospective identification of tumorigenic breast cancer cells. *Proc. Natl. Acad. Sci. U.S.A. 100*, 3983−3988.
(38) Sheridan, C., Kishimoto, H., Fuchs, R. K., Mehrotra, S., Bhat-Nakshatri, P., Turner, C. H., Goulet, R., Jr., Badve, S., and Nakshatri, H. (2006) CD44+/CD24- breast cancer cells exhibit enhanced invasive properties: an early step necessary for metastasis. *Breast Cancer Res. 8*, R59.
(39) Ekici, S., Cerwinka, W. H., Civantos, F., Soloway, M. S., and Lokeshwar, V. B. (2004) Comparison of the prognostic potential of hyaluronic acid, hyaluronidase(HYAL-1), CD44v6 and microvessel density for prostate cancer. *Int. J. Cancer 112*, 121−129.
(40) Udabage, L., Brownlee, G. R., Nilsson, S. K., and Brown, T. J. (2005) The over-expression of HAS2, Hyal-2 and CD44 is implicated in the invasiveness of breast cancer. *Exp. Cell Res. 310*, 205−217.
(41) Choi, K. Y., Min, K. H., Yoon, H. Y., Kim, K., Park, J. H., Kwon, I. C., Choi, K., and Jeong, S. Y. (2011) PEGylation of hyaluronic acid nanoparticles improves tumor targetability in vivo. *Biomaterials 32*, 1880−1889.
(42) Liu, Y., Sun, J., Cao, W., Yang, J., Lian, H., Li, X., Sun, Y., Wang, Y., Wang, S., and He, Z. (2011) Dual targeting folate-conjugated hyaluronic acid polymeric micelles for paclitaxel delivery. *Int. J. Pharm. 421*, 160−169.
(43) Mishra, A., Mishra, A., Behera, R. K., Behera, R. K., Behera, P. K., Behera, P. K., Mishra, B. K., Mishra, B. K., Behera, G. B., and Behera, G. B. (2000) Cyanines during the 1990s: A Review. *Chem. Rev. 100*, 1973−2012.
(44) Saxena, V., Sadoqi, M., and Shao, J. (2004) Indocyanine green-loaded biodegradable nanoparticles: preparation, physicochemical characterization and in vitro release. *Int. J. Pharm. 278*, 293−301.
(45) Yoon, H. K., Ray, A., Lee, Y. E., Kim, G., Wang, X., and Kopelman, R. (2013) Polymer-protein hydrogel nanomatrix for stabilization of indocyanine green towards targeted fluorescence and photoacoustic bio-imaging. *J. Mater. Chem. B: Mater. Biol. Med. 1*, 1−19.
(46) Yu, J., Yaseen, M. A., Anvari, B., and Wong, M. S. (2007) Synthesis of near-infrared-absorbing nanoparticle-assembled capsules. *Chem. Mater. 19*, 1277−1284.
(47) Saxena, V., Sadoqi, M., and Shao, J. (2004) Enhanced photo-stability, thermal-stability and aqueous-stability of indocyanine green in polymeric nanoparticulate systems. *J. Photochem. Photobiol. 74*, 29−38.
(48) Dubois, A., Canva, M., Brun, A., Chaput, F., and Boilot, J. P. (1996) Photostability of dye molecules trapped in solid matrices. *Appl. Opt. 35*, 3193−3199.
(49) Mok, H., Jeong, H., Kim, S.-J., and Chung, B. H. (2012) Indocyanine green encapsulated nanogels for hyaluronidase activatable and selective near infrared imaging of tumors and lymph nodes. *Chem. Commun. 48*, 8628−8630.
(50) Ogawa, M., Kosaka, N., Longmire, M. R., Urano, Y., Choyke, P. L., and Kobayashi, H. (2009) Fluorophore-quencher based activatable targeted optical probes for detecting in vivo cancer metastases. *Mol. Pharmaceutics 6*, 386−395.
(51) Beziere, N., Lozano, N., Nunes, A., Salichs, J., Queiros, D., Kostarelos, K., and Ntziachristos, V. (2014) Dynamic imaging of PEGylated indocyanine green (ICG) liposomes within the tumor microenvironment using multi-spectral optoacoustic tomography (MSOT). *Biomaterials 37C*, 415−424.
(52) Marshall, M. V., Draney, D., Sevick-Muraca, E. M., and Olive, D. M. (2010) Single-dose intravenous toxicity study of IRDye 800CW in Sprague-Dawley rats. *Mol. Imaging Biol. 12*, 583−594.
(53) Ott, P. (1998) Hepatic elimination of indocyanine green with special reference to distribution kinetics and the influence of plasma protein binding. *Pharmacol. Toxicol. 83* (Suppl 2), 1−48.
(54) Miki, K., Inoue, T., Kobayashi, Y., Nakano, K., Matsuoka, H., Yamauchi, F., Yano, T., and Ohe, K. (2014) Near-infrared dye-conjugated amphiphilic hyaluronic acid derivatives as a dual contrast agent for in vivo optical and photoacoustic tumor imaging. *Biomacromolecules 16*, 219−227.
(55) Dvorak, H. F. (2010) Vascular permeability to plasma, plasma proteins, and cells: an update. *Curr. Opin. Hematol. 17*, 225−229.

DOI: 10.1021/bc5005679
Bioconjugate Chem. 2015, 26, 294−303